nature communications

Article

https://doi.org/10.1038/s41467-025-60400-5

Boosting oxygen reduction performances in Pd-based metallenes by co-confining interstitial H and *p*-block single atoms

Received: 6 November 2024

Accepted: 20 May 2025

Published online: 06 June 2025

Check for updates

Yu Qiu[1,6], Mingzi Sun[2,3,6], Jiandong Wu[1,4], Chunxiao Chai[5], Shengwei Wang[1], Hong Huang[1], Xiao Zhao[1], Dongxu Jiao[1], Shan Xu[1], Dewen Wang[1], Xin Ge[1], Wei Zhang[1], Weitao Zheng[1], Yujiang Song[5], Jinchang Fan[1] ✉, Bolong Huang[2,3] ✉ & Xiaoqiang Cui[1] ✉

The efficiency of the oxygen reduction reaction (ORR) is limited by the scaling relationship in the conventional oxygen associative pathway. To break such limitations, we present an approach to effectively activate the oxygen dissociative pathway through co-confining single *p*-block (In, Sn, Pb) atoms and interstitial H atoms within Pd metallenes, leading to good ORR performance. $PdPbH_x$ metallenes exhibit a high mass activity of 1.36 A mg^{-1} at 0.95 V (vs. RHE), which is 46.9 times higher than that of the benchmark Pt/C. The minimal performance decay after 50,000 potential cycles confirms a good stability. In situ vibrational spectroscopy investigations and theoretical calculations highlight that interstitial H atoms facilitate the direct dissociation of O_2 while single Pb atoms enhance O_2 adsorption strength. The electroactive $PdPbH_x$ metallenes is attributed to the up-shifted Pd-4*d* orbitals induced by H and Pb atoms. This research supplies critical inspiration for developing highly efficient ORR electrocatalysts.

Fuel cells hold immense potential as a pristine and efficient energy technology, offering zero carbon emissions, elevated energy efficiency, and reduced operating temperatures[1–3]. However, the sluggish reaction kinetics of the cathodic oxygen reduction reaction (ORR) pose a significant obstacle in electrocatalysis, hindering the widespread adoption of commercial fuel cells[4,5]. This challenge is primarily ascribed to the multiple proton-coupled electron transfer steps and corresponding oxygen-containing intermediates involved in the ORR process[6–9]. Specifically, most electrocatalysts exhibit an oxygen-associative mechanism that involves the adsorption of three intermediates: superoxide ($^*OOH$), hydroxyl ($^*OH$), and oxygen atom ($^*O$)[10–17]. These intermediates exhibit the scaling relationship of $\Delta G_{^*OOH} \approx \Delta G_{^*OH} + 3.2$ eV and $\Delta G_{^*O} \approx 2\Delta G_{^*OH}$[8,18]. Consequently, optimizing the binding energy of each intermediate independently becomes a great challenge, resulting in a high theoretical overpotential required to drive the ORR process and subsequently diminishing ORR activity[6,19,20]. According to the well-established ORR free energy diagram, the rate-determining step (RDS) in ORR is either $O_2 \rightarrow {}^*OOH$ or $^*OH \rightarrow H_2O$[7]. Considering that the $^*OH \rightarrow H_2O$ step is unavoidable during the ORR process, there is a critical need for a practical approach that bypasses $^*OOH$ formation and directly dissociates the adsorbed oxygen molecule ($^*O_2$) into two $^*O$ species to further enhance ORR performance[21,22]. Nevertheless, achieving this objective entails the development of an efficient electrocatalyst with

[1]School of Materials Science and Engineering, Key Laboratory of Automobile Materials of MOE, Electron Microscopy Center, Jilin University, 2699 Qianjin Street, Changchun 130012, China. [2]Department of Chemistry, City University of Hong Kong, Kowloon, Hong Kong SAR, China. [3]Department of Applied Biology and Chemical Technology, The Hong Kong Polytechnic University, Hung Hom, Kowloon, Hong Kong SAR, China. [4]Key Laboratory of Pathobiology of MOE, Nanomedicine and Translational Research Center, The Third Bethune Hospital of Jilin University, 126 Sendai Street, Changchun 130033, China. [5]State Key Laboratory of Fine Chemicals, School of Chemical Engineering, Dalian University of Technology, 2 Linggong Road, Dalian 116024, China. [6]These authors contributed equally: Yu Qiu, Mingzi Sun. ✉e-mail: jcfan@jlu.edu.cn; b.h@cityu.edu.hk; xqcui@jlu.edu.cn

robust O_2 adsorption capability, which is a longstanding challenge that persists in the field.

Two-dimensional metallenes, distinguished by their large specific surface area, high electrical conductivity, and maximized atomic utilization, are promising candidates in the domain of ORR[23–27]. Moreover, their adjustable microscopic structures make them an ideal platform for regulating the reaction mechanisms[28,29]. Prior research has explored diverse strategies such as alloying[30,31], defect engineering[32,33], and surface strain[25,34] to modulate the *d*-band center of active sites in metallenes, thereby controlling their binding energies with oxygen-containing intermediates and improving ORR performances. However, it should be noted that the strong attractive interactions between surface atoms in metallenes inherently generate a compressed strain[34], which results in relatively low binding energy with $^*O_2$. This induces a significant challenge in triggering the oxygen dissociation pathway within metallenes, as it requires overcoming a moderate energy barrier.

Herein, we present a series of highly efficient catalysts of Pd-based metallenes for alkaline ORR achieved by co-confining single *p*-block (In, Sn, Pb) atoms in the sub-surface and interstitial H atoms within the lattice of Pd metallenes. Among them, $PdPbH_x$ metallenes exhibit a high mass activity of 1.36 A mg^{-1} at 0.95 V (vs. RHE), which is 46.9 times higher than that of commercial Pt/C and shows a competitive performance with previous works on Pd-based catalysts. Notably, the $PdPbH_x$ metallenes demonstrate negligible activity decay even after undergoing 50,000 potential cycles, exhibiting no observable changes in structure and composition. In situ attenuated total reflection Fourier transform infrared (ATR-FTIR) spectroscopy analysis reveals that interstitial H atoms induce the oxygen dissociative pathway, while the confined single Pb atoms further enhance the pathway by promoting stronger O_2 adsorption. Density functional theory (DFT) calculations elucidate that the improved electroactivity of Pd sites is potentially attributed to the introduction of interstitial H and single Pb atoms, which facilitates the adsorption of crucial intermediates and accelerates the electron transfer to promote the direct dissociation of O_2. Additionally, the improved *p*-*d* overlapping improves the selectivity of the oxygen dissociative pathway due to the decreased energy barriers, leading to high ORR performance.

Results

Morphology and structure characterizations

Building on the fact that *p*-block elements exhibit good miscibility with Pd and can form various solid solutions with Pd (Supplementary Fig. 1), a series of $PdMH_x$ (M= In, Sn, Pb) metallenes were synthesized using a seed-mediated method, as illustrated in Fig. 1a and Supplementary Fig. 2. In this process, Pd and M ions were co-reduced epitaxially on the surface of Pd metallene seeds to form PdM metallenes with a defect-rich structure. The Pd atoms located at the defect areas of PdM metallenes exhibit higher energy and increased activity, making them susceptible to oxidation and etching by residual air[35]. These Pd atoms are subsequently re-deposited on the surface and edges of the PdM metallenes, effectively burying the M atoms within the lattice. As the Pd atoms from the interior and edges of the defect areas migrate, the pores gradually expand. Meanwhile, hydrogen atoms generated in situ from the decomposition of N,N-dimethylformamide (DMF) permeate into the lattice of PdM during the etching process, resulting in the formation of $PdMH_x$ nanorings (Supplementary Figs. 2–8).

The morphology of the $PdMH_x$ metallenes was characterized using transmission electron microscopy (TEM) and high-angle annular dark-field scanning transmission electron microscopy (HAADF-STEM). As a typical structure, $PdPbH_x$ metallenes show the interconnected ring-like shape (Fig. 1b, c), with a thickness of 3.93 ± 0.2 nm by analyzing the atomic force microscopy (AFM) images and corresponding height profiles (Fig. 1d). The observed reduction in the hole size of the nanorings in AFM images relative to TEM images is predominantly a consequence of the tip effect inherent to AFM measurements[36,37]. Energy dispersive X-ray spectroscopy (EDS) elemental mapping demonstrated the uniform distribution of Pd and Pb elements in the $PdPbH_x$ metallenes, confirming their alloy feature (Fig. 1e). The Pd/Pb atomic ratio, determined based on EDS results, was found to be 91.3/8.7 (Supplementary Table 1), which was consistent with the data obtained from inductively coupled plasma atomic emission spectroscopy (ICP-AES, Supplementary Table 2). Furthermore, atomic-resolution HAADF-STEM images and corresponding intensity profiles (Fig. 1f, g) revealed that the atomic structure of the $PdPbH_x$ metallenes consisted of relatively bright spots (high peak intensity) and numerous relatively dark spots (low peak intensity). Given the higher atomic number of Pb (Z = 82) compared to Pd (Z = 46), the brighter spots were attributed to Pb atoms, while the darker spots were attributed to Pd atoms. Importantly, the Pb atoms were found to be atomically dispersed within the Pd lattice without any Pb-Pb bonds, indicating a single-atom alloy feature. Notably, the $PdInH_x$ and $PdSnH_x$ metallenes show a similar ring-like morphology and single-atom alloy structure to that of the $PdPbH_x$ metallenes (Supplementary Figs. 9 and 10), demonstrating the universality of the synthetic method.

Structural and electronic properties

Figure 2a presents the X-ray diffraction (XRD) results, which show that the peaks of $PdPbH_x$ metallenes shift to a lower angle compared to Pd metallenes. This shift is in line with the standard PdH_x phase (PDF#87-0637) with the H content of 0.32 (Supplementary Fig. 11), confirming the formation of metal hydride. In addition, we have plotted a standard curve of the relationship between the lattice constant and Pb content within *fcc*-Pd_xPb_{1-x} alloys, demonstrating that the XRD peak shift of $PdPbH_x$ is mainly due to the incorporation of interstitial hydrogen atoms instead of Pb atoms (Supplementary Fig. 12). H solid-state nuclear magnetic resonance (ssNMR) was conducted to further investigate the presence of interstitial H atoms. Figure 2b shows a new peak at 26.1 ppm in the ^1H solid state nuclear magnetic resonance (ssNMR) spectrum of $PdPbH_x$ metallenes, indicating the formation of the Pd-H bonds[38,39]. The interaction between Pd and H atoms was also confirmed by electron energy loss spectroscopy (EELS) (Fig. 2c) and X-ray photoelectron spectroscopy (XPS) results (Supplementary Fig. 13), which demonstrate that $PdPbH_x$ metallenes exhibit a lower EELS peak energy and a narrower valence band compared to Pd metallenes. These observations are consistent with the behavior observed in palladium hydride systems[40,41].

X-ray absorption spectroscopy (XAS) was employed to study the coordination environments and chemical states of Pd and Pb atoms in $PdPbH_x$ metallenes. Figure 2d displays the X-ray absorption near-edge structure (XANES) spectra of Pd K-edge in $PdPbH_x$ metallenes, in which the adsorption edge in $PdPbH_x$ metallenes is close to that in the Pd foil, demonstrating that the Pd atoms in $PdPbH_x$ metallenes are mainly in the metallic state. The conclusion was consistent with XPS results (Supplementary Fig. 14). The coordination situation of Pd atoms in $PdPbH_x$ metallenes was further investigated by Fourier transform extended X-ray absorption fine structure (FT-EXAFS) and wavelet transform EXAFS (WT-EXAFS) (Fig. 2e, f and Supplementary Fig. 15). Figure 2e displays that the EXAFS at the Pd K-edge spectra of $PdPbH_x$ metallenes is the same as that of Pd foil, meaning the crystal structure remains unchanged after doping. The Pd-Pd/Pb bond length in $PdPbH_x$ metallenes was measured to be 2.82 Å (Fig. 2e, f and Supplementary Table 3), which is 0.08 Å longer than that in Pd foil (2.74 Å) due to the existence of interstitial H atoms[24]. XANES spectra of Pb L_3-edge indicate that Pb atoms in $PdPbH_x$ metallenes are primarily in the metallic state (Fig. 2g). The FT-EXAFS and WT-EXAFS results (Fig. 2h, i, Supplementary Fig. 16) show that the Pb component in the $PdPbH_x$ metallenes only exhibits one peak of Pb-Pd bond, indicating that Pb atoms are atomically dispersed in the Pd lattice without aggregations. Additionally, the EXAFS fitting results of $PdPbH_x$ metallenes reveal a

coordination number of approximately 9.1 for the Pb-Pd bond, slightly higher than that for the Pd-Pd bond with a value of 7.2 (Supplementary Table 3). This suggests that Pb atoms are mainly located in the interior area with a large coordination number. Conversely, XAS analysis of PdPb metallenes indicates that Pb atoms are distributed throughout the entire structure, including both the internal and exterior regions. (Supplementary Figs. 17–19). These inferences are further supported by the galvanic replacement experiment, where Cu was used to replace surface Pb atoms (Supplementary Table 4)[23,33]. XPS results (Supplementary Fig. 20) confirm that Pb atoms are confined within the internal region of $PdPbH_x$ metallenes, whereas Pb atoms are located outside PdPb metallenes rather than being confined solely within the internal region.

Evaluation of ORR performance

The electrocatalytic performance of $PdPbH_x$ metallenes for ORR was evaluated using a rotating disk electrode (RDE) measurement and compared to commercial Pt/C as the benchmark. Before the test, $PdPbH_x$ metallenes, PdH_x metallenes (a comparison sample without the Pb element, Supplementary Fig. 21), and PdPb metallenes were deposited onto the carbon black support. Cyclic voltammetry (CV) curves were measured for these catalysts in a N_2-saturated 0.1 M KOH solution at a scan rate of 50 mV s^{-1}. The electrochemical active surface areas (ECSA), which provide an estimate of the available active sites for the ORR process, were calculated based on the integral calculation of the reduction peak areas of Pd-oxides. Figure 3a shows that $PdPbH_x$ metallenes/C exhibits the highest ECSA value and the most positive Pd-O peak potential compared to the other three catalysts (Supplementary Table 5, Supplementary Figs. 22 and 23). This observation indicates that $PdPbH_x$ metallenes possess a significant number of active sites, primarily located on steps and ledges within the nanoring structure[42–44]. Additionally, the CV curves of all samples at a scan rate of 10 mV s^{-1} showed both $PdPbH_x$ and PdPb exhibited lower current densities at 1.3 V during the positive sweep compared to PdH_x (Supplementary Fig. 24), indicating that the introduction of Pb can reduce the oxidation degree at high potentials[45]. Furthermore, the ORR

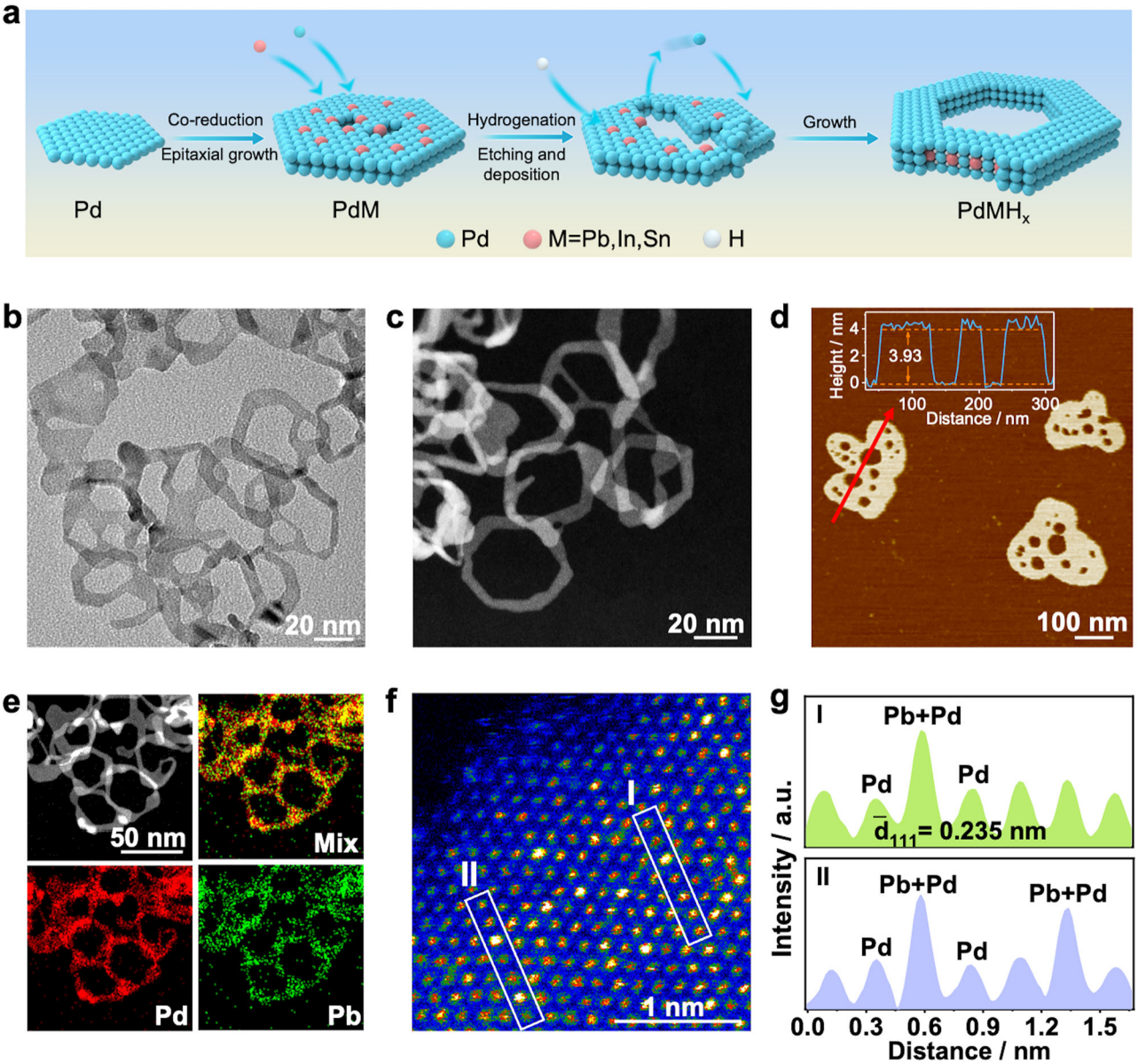

Fig. 1 | Morphology and structure characterizations of $PdPbH_x$ metallenes. **a** Scheme of the synthesis process of $PdMH_x$ metallenes. **b** TEM image, (**c**) HAADF-STEM image, (**d**) AFM image and corresponding height profile, (**e**) EDS-mapping images, (**f**) atomic-resolution rainbow-colored HAADF-STEM image of $PdPbH_x$ metallenes. **g** The measured atomic intensity line scanning profile along the rectangles labeled in (**f**). Source data are provided as a Source Data file.

https://doi.org/10.1038/s41467-025-60400-5

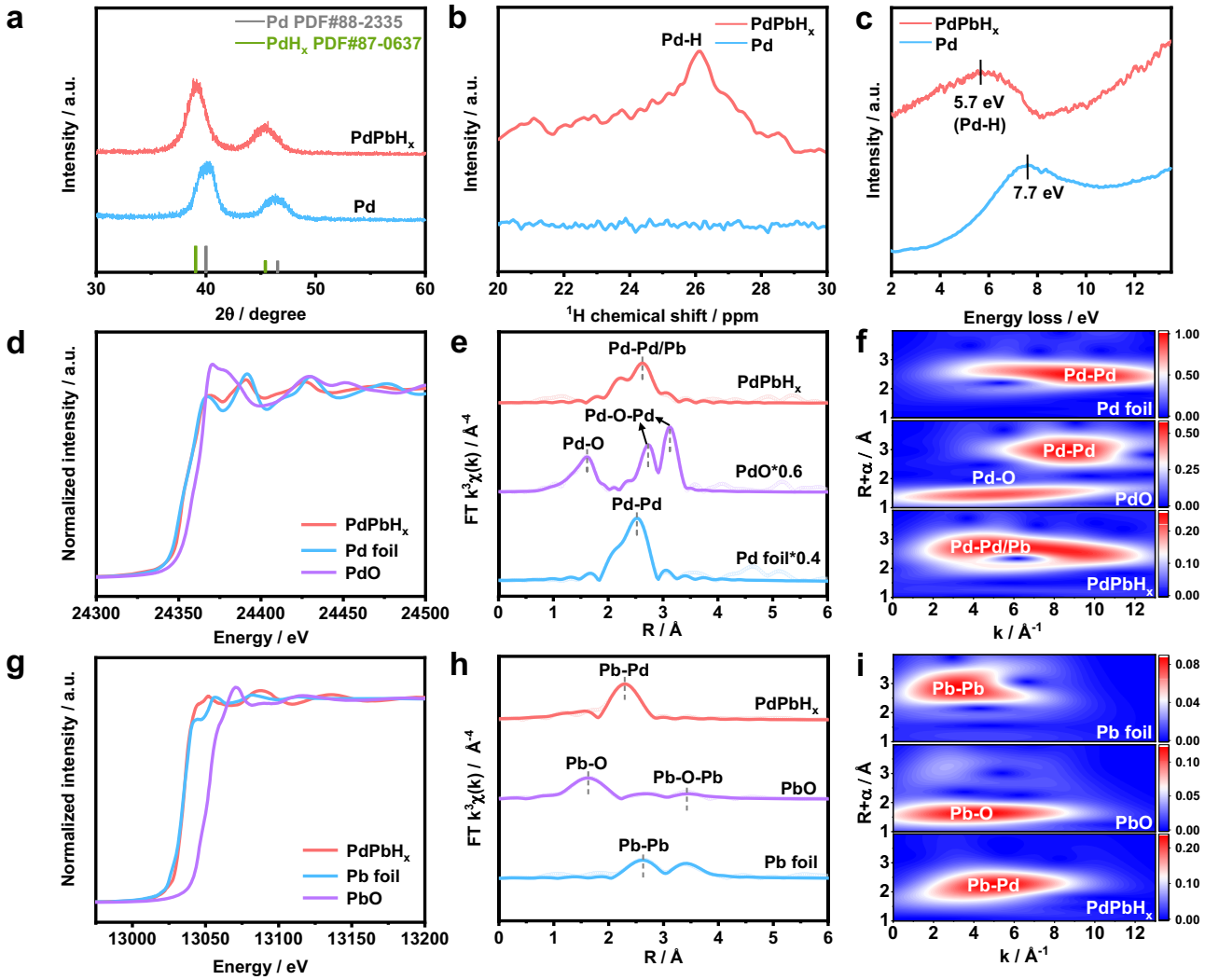

Fig. 2 | Structural and electronic properties of $PdPbH_x$ metallenes. a XRD patterns, (**b**) ^{1}H ssNMR spectra, (**c**) EELS spectra of $PdPbH_x$ metallenes and Pd metallenes. **d** Pd K-edge XANES, (**e**) EXAFS spectra and (**f**) WT contour maps of $PdPbH_x$ metallenes and standard samples of Pd foil and PdO. **g** Pb L_3-edge XANES, (**h**) EXAFS spectra and (**i**) WT contour maps of $PdPbH_x$ metallenes and standard samples of Pb foil and PbO. Source data are provided as a Source Data file.

polarization curves were measured in an O_2-saturated 0.1 M KOH solution at a scan rate of 10 mV s^{-1}. As shown in Fig. 3b, the half-wave potential ($E_{1/2}$) in $PdPbH_x$ metallenes/C is 0.958 V, which is much more positive than that in PdH_x metallenes/C (0.910 V), PdPb metallenes/C (0.907 V), and commercial Pt/C (0.845 V). Noting that the LSV curves in Fig. 3b are the positive scan from 0.3 V to 1.1 V (Step I), which is higher to that observed during the negative scan from 1.1 V to 0.3 V (Step II) (Supplementary Fig. 25). This difference can be attributed to the reaction of Pd/Pt with OH^- at high potentials, forming inactive Pd/Pt-based oxides[46]. However, the LSV curves (Step III) revert to the one observed in Step I, indicating that the Pd/Pt-based oxides may be electrochemically reduced back to their original active metal state under these test conditions. Additionally, quasi in situ XPS results show that the area ratio of $Pd^{2+}/Pd^{2+}+Pd^0$ always keeps below 0.25 across the whole testing potential (Supplementary Fig. 26), indicating the Pd in $PdPbH_x$ metallenes remained predominantly in its metallic state throughout the ORR process. The Tafel slope of $PdPbH_x$ metallenes/C is 59.8 mV dec^{-1}, which is much lower than that of PdH_x metallenes/C with 68.5 mV dec^{-1}, PdPb metallenes/C with 88.9 mV dec^{-1}, and commercial Pt/C with 101.3 mV dec^{-1} (Fig. 3c), suggesting the faster ORR reaction kinetics on $PdPbH_x$ metallenes/C among the four samples[10]. By applying the Koutecky-Levich equation to analyze polarization curves, the catalytic kinetic currents were calculated. These values are subsequently normalized using both the metal loading mass and ECSA to determine the mass activity (MA) and specific activity (SA) (Fig. 3d). Since the universally chosen potential (0.9 V) is too close to the diffusion limit region to provide reliable dynamic current density due to the fast kinetic of $PdPbH_x$ metallenes/C (Supplementary Fig. 27), we evaluated the activity at 0.95 V to eliminate the O_2 diffusion limit[23,47]. As shown in Fig. 3d, at 0.95 V, $PdPbH_x$ metallenes/C exhibited outstanding MA (1.36 A mg^{-1}_{Pd}) and SA (1.59 mA cm^{-2}), which are 46.9-fold and 31.9-fold enhancements compared to commercial Pt/C, respectively. Optimization experiments for ORR performance with varying Pb doping amounts revealed that the synthesized $PdPbH_x$ catalyst with a Pb atomic ratio of 8.7% exhibited better performance (Supplementary Fig. 28). Additionally, the ORR performance of $PdPbH_x$ metallenes was evaluated in acidic electrolytes, also showing much better activity compared to commercial Pt/C (Supplementary Fig. 29 and Supplementary Table 6). These results indicate the superior electrocatalytic activity of $PdPbH_x$ metallenes/C for the ORR compared to the other catalysts studied. Notably, when alloyed single atoms are changed into In and Sn, these hydride bimetallenes materials also exhibit good ORR performance (Supplementary Figs. 30, 31), highlighting the versatility of this strategy for enhancing ORR activity through the co-confinement of single *p*-block and interstitial H atoms in Pd-based metallenes.

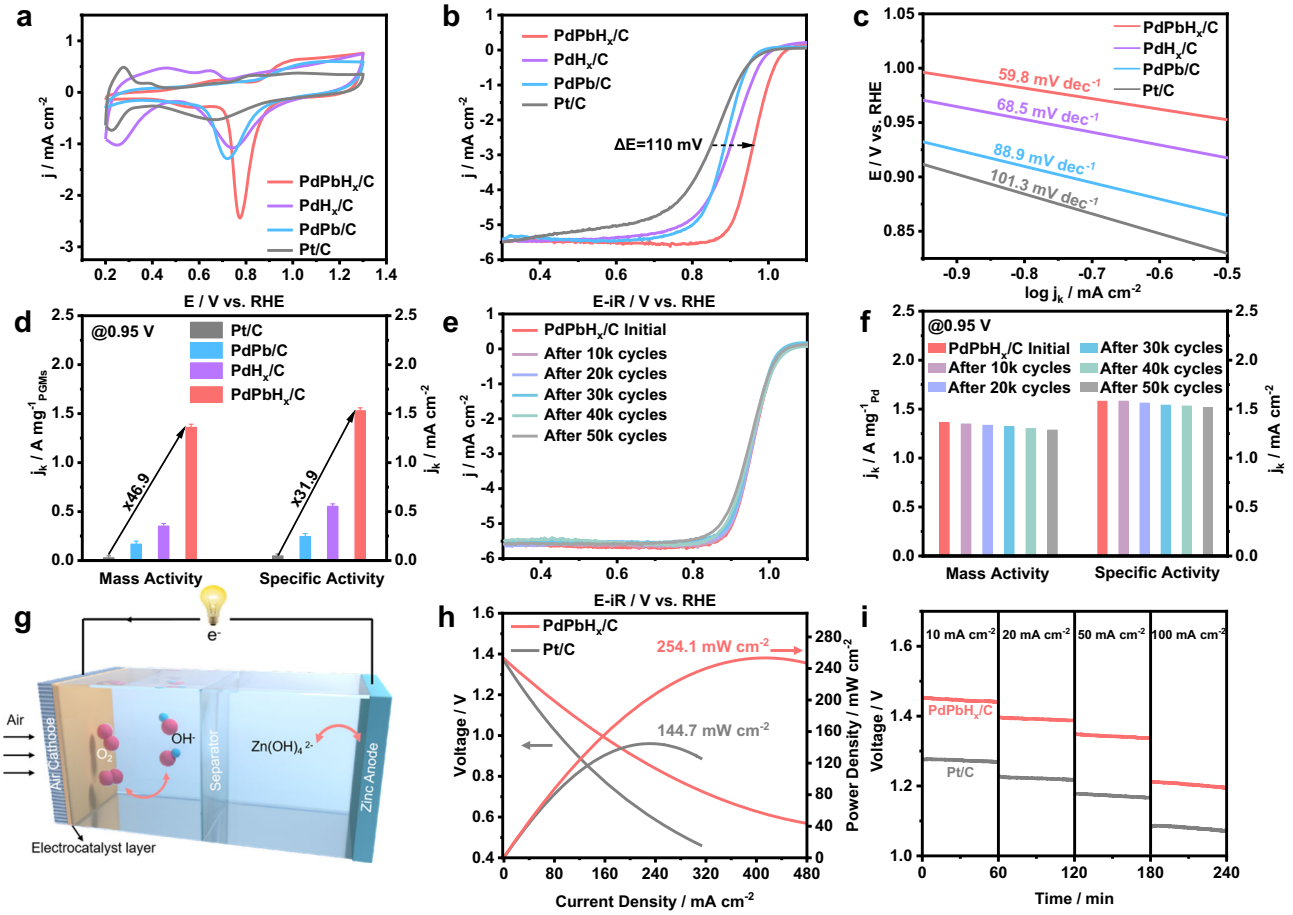

Fig. 3 | Electrocatalytic performance of $PdPbH_x$ metallenes/C, PdH_x metallenes/C, PdPb metallenes/C and commercial Pt/C catalysts. a CV curves recorded in N_2-saturated 0.1 M KOH solutions at 25 °C with a scan rate of 50 mV s^{-1}. **b** ORR polarization curves recorded in O_2-saturated 0.1 M KOH electrolyte at 25 °C, with a rotation rate of 1600 rpm and a positive scan rate of 10 mV s^{-1}. **c** Corresponding Tafel plots. **d** The comparisons in mass activity and specific activity at 0.95 V. The error bars represent the standard deviation derived from three independent experimental measurements. **e** Durability performance of LSV evolutions of $PdPbH_x$ metallenes/C. **f** The changes in mass activities and specific activities of $PdPbH_x$ metallenes/C catalyst before and after the durability test for various potential-scanning cycles. Noting that the area value used for current density normalization (mA cm^{-2}) was 0.196 cm^2 corresponding to the glassy carbon substrate support area. The solution resistance (R_s = 40 ± 5 Ω) was obtained from EIS measurements. **g** Schematic illustration of ZABs. **h** Discharge and power density curves, **i** Galvanostatic discharge curves at current densities from 10 to 100 mA cm^{-2} of $PdPbH_x$ metallenes/C and commercial Pt/C. Source data are provided as a Source Data file.

To assess the electrochemical durability of $PdPbH_x$ metallenes/C, the accelerated stability test was conducted in an O_2-saturated 0.1 M KOH solution between 0.6 and 1.0 V versus RHE at a scan rate of 200 mV s^{-1}. Remarkably, after 50,000 cycles, the half-wave potential ($E_{1/2}$) of $PdPbH_x$ metallenes/C exhibited a slight decrease of 8 mV, indicating good stability (Fig. 3e). ECSAs measured before and after 50,000 potential cycles remain at a high value without evident changes (Supplementary Fig. 32). The MA and SA of $PdPbH_x$ metallenes/C also remained at 95% and 96% of their initial values after 50,000 cycles, respectively (Fig. 3f). In contrast, the ORR activity of PdH_x metallenes/C, PdPb metallenes/C, and commercial Pt/C decreased notably after 50,000 cycles (Supplementary Fig. 33). The long-term chrono-amperometry measurements were conducted at 0.6 V vs. RHE for $PdPbH_x$ metallenes/C and commercial Pt/C (Supplementary Fig. 34). The results showed that the $PdPbH_x$ metallenes/C maintains approximately 90.6% of its initial current density after testing for 30,000 s, whereas commercial Pt/C only can maintain 33.7%, demonstrating the extraordinary durability of $PdPbH_x$ metallenes compared to commercial Pt/C. Furthermore, the morphology, single atom alloy feature, and hydride nature of $PdPbH_x$ metallenes were retained after the accelerated stability measurement, as confirmed by imaging techniques (Supplementary Figs. 35–37, Table 1 and 2). The ORR performance of $PdPbH_x$ metallenes, including the mass activity and long-term stability, surpasses those of the recently reported Pd-based ORR catalysts under alkaline media (Supplementary Table 7). Simultaneously, the half-wave potential and mass activity at 0.95 V vs. RHE of $PdPbH_x$ metallenes also surpass those of most reported high-activity M-N-C materials. (Supplementary Table 8). In comparison, PdH_x metallenes/C displayed noticeable morphology changes and substantial aggregation after 50,000 cycles (Supplementary Fig. 38). This enhanced durability of $PdPbH_x$ metallenes can be attributed to the unique nanoring structure, which exhibits a stronger binding force with the carbon support. The corresponding stability of the electrocatalysts has also been verified by molecular dynamics (MD) simulations at room temperature, where both PdPb and PdH_x show much reduced stability due to the strong structural distortions (Supplementary Fig. 39). In comparison, the $PdPbH_x$ is much more stable. Importantly, the synthesis of $PdPbH_x$ metallenes can be easily scaled up to produce larger quantities without significant changes in crystal structures and catalytic performances, supporting the practical applicability of $PdPbH_x$ for future applications (Supplementary Fig. 40). To further validate the good ORR performances of $PdPbH_x$ metallenes, practical Zn-air batteries (ZABs) and H_2-O_2 AEMFC tests were conducted with fuel cell devices containing $PdPbH_x$ metallenes/C and commercial Pt/C as a cathode catalyst material. For ZABs performance, compared to the

https://doi.org/10.1038/s41467-025-60400-5

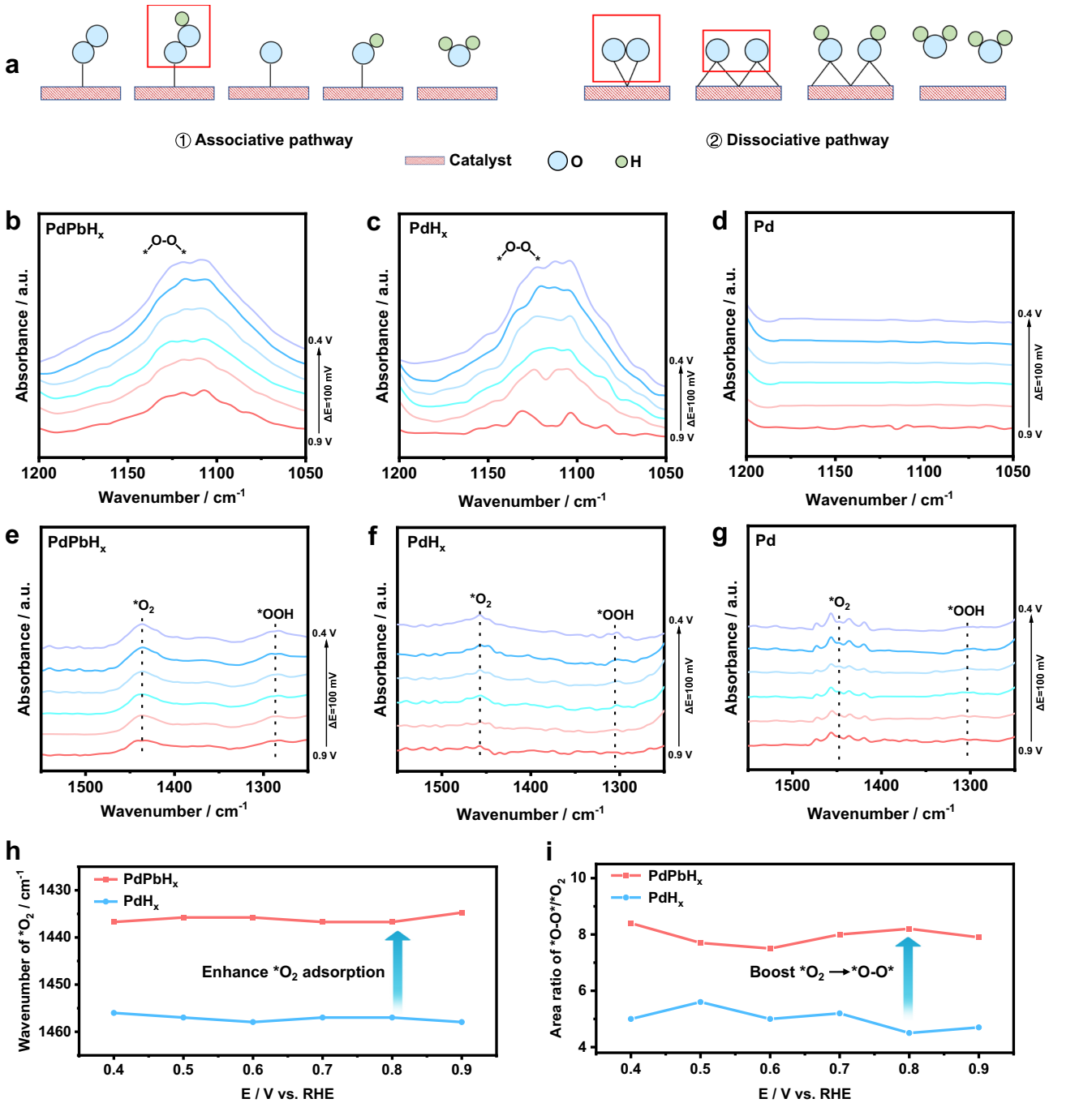

Fig. 4 | The exploration of ORR mechanism for catalysts via in situ ATR-FTIR spectra. a The schematic diagram of the O_2 associative pathway and the O_2 dissociative pathway. In situ ATR-IR spectra under applied potentials in O_2-saturated 0.1 M KOH in the wavenumber range (1050–1200 cm^{-1}) of (**b**) $PdPbH_x$ metallenes/C, (**c**) PdH_x metallenes/C, (**d**) Pd metallenes/C, and in the wavenumber range (1250–1550 cm^{-1}) of (**e**) $PdPbH_x$ metallenes/C, (**f**) PdH_x metallenes/C, (**g**) Pd metallenes/C. **h** The statistic of $^*O_2$ peak position of $PdPbH_x$ metallenes/C and PdH_x metallenes/C under different potentials, obtained from (**e**, **f**). **i** The area ratio of $^*O\text{-}O^*/^*O_2$ peak of $PdPbH_x$ metallenes/C and PdH_x metallenes/C, obtained from the integral of $^*O\text{-}O^*/^*O_2$ peak area in (**b**, **e**) and (**c**, **f**). Source data are provided as a Source Data file.

commercial Pt/C, $PdPbH_x$ metallenes/C exhibit higher open-circuit voltage (1.55 V), power density (254.1 mW cm^{-2}) and specific capacity (794.1 mAh per gram Zn) (Fig. 3g, h and Supplementary Fig. 41). We also examined the rate capability of our $PdPbH_x$ metallenes/C at different current densities, further demonstrating the potential of $PdPbH_x$ metallenes/C as air cathodes for practical applications (Fig. 3i). The H_2-O_2 fuel cell utilizing $PdPbH_x$ metallenes/C achieved a peak power density of 722 mW cm^{-2} at a loading of 0.3 mg cm^{-2}, surpassing the Pt/C-based systems (589 mW cm^{-2}) (Supplementary Fig. 42).

Mechanistic studies via in situ ATR-FTIR spectroscopy

The four-electron ORR process involves two fundamental pathways as shown in Fig. 4a and summarized in Supplementary Table 9[48,49]. The first pathway is the oxygen associative mechanism, where $^*OOH$ intermediates are formed through the protonation of $^*O\text{-}O$. The second pathway is the oxygen dissociative mechanism, where $^*O\text{-}O^*$ directly dissociates into two $^*OH$ species, followed by continuous protonation. Consequently, different ORR mechanisms can be distinguished by specific reaction intermediates: $^*O\text{-}O^*$ species indicate the dissociative mechanism while the $^*OOH$ intermediate represents the associative

mechanism. In situ ATR-FTIR spectroscopy was then performed to identify reaction intermediates and investigate the ORR mechanism on different metallene-based catalysts (Supplementary Fig. 43). In the wavenumber range of 1050–1200 cm^{-1}, a peak around 1175 cm^{-1} corresponding to the $^*O$-O^* species was observed on $PdPbH_x$ metallenes/C and PdH_x metallenes/C (Fig. 4b and c)[50], while no obvious adsorption peak is observed in this region on Pd metallenes/C and PdPb metallene/C (Fig. 4d and Supplementary Fig. 44). The results indicate the dissociative pathway is exclusively occurred on the hydride metallenes, highlighting the unique role of interstitial H atoms in inducing the oxygen dissociation pathway. Notably, the peak around 1300 cm^{-1} corresponds to the O-O stretching mode of $^*OOH$ intermediate[51,52] is observed on all metallene-based catalysts, indicating the presence of the oxygen associative pathways during the ORR process (Fig. 4e–g). To further elucidate the influence of doped Pb atoms, the wavenumber of the O_2 adsorption peak (within the range of approximately 1430–1470 cm^{-1})[52,53] and the integral area ratio of the $^*O$-O^*/$^*O_2$ peak was systematically analyzed for both $PdPbH_x$ metallenes/C and PdH_x metallenes/C. As displayed in Fig. 4h, the wavenumber of the $^*O_2$ peak in $PdPbH_x$ metallenes/C is significantly lower than that in PdH_x metallenes/C under all applied potentials, suggesting a stronger O_2 adsorption energy on the former catalyst. Furthermore, the integral area ratio of the $^*O$-O^*/$^*O_2$ peak in $PdPbH_x$ metallenes/C is higher compared to that in PdH_x metallenes/C during the entire ORR process (Fig. 4i). In summary, Pb atoms in $PdPbH_x$ metallenes enhance the adsorption strength of O_2 molecules on the catalyst surface and facilitate the activation process of $^*O_2$ to $^*O$-O^*, thereby promoting the oxygen dissociative process and improving ORR performances in $PdPbH_x$ metallenes/C.

Theoretical calculations

Detailed theoretical investigations regarding the electronic structures and reaction trends for ORR were carried out to explore the outstanding ORR performances of $PdPbH_x$ metallenes. For demonstrating the electroactivity differences, the distributions of bonding and anti-bonding orbitals near the Fermi level (E_F) for PdPb, PdH_x, and $PdPbH_x$ surfaces were first compared (Fig. 5a–c, Supplementary Fig. 45). For the (111) surface of the PdPb, the bonding orbitals only partially distribute on the surface while the anti-bonding orbitals are slightly more dominant, which supplies limited electroactive sites to guarantee efficient electron transfer during the ORR (Fig. 5a). For PdH_x, although the bonding orbitals become more evident on unsaturated Pd sites of the edge, the overall anti-bonding distributions are still dominant on the surface (Fig. 5b). With the introduction of Pb, the electronic distributions of $PdPbH_x$ are evidently optimized, where the surface sites are mainly dominated by the bonding orbitals, offering a highly electroactive surface to enable efficient adsorption of oxygen and accelerate electron transfer (Fig. 5c). The projected partial density of states (PDOS) is further compared to understand the electronic structures of different electrocatalysts. For the PdPb surface, the Pd-4*d* orbitals exhibit a relatively broad distribution with continuous peaks, covering from E_V-6.0 eV to E_V (E_V denotes 0 eV) (Fig. 5d). For Pb sites, the 6*s* orbitals show limited contributions, which are located far from the E_F. In contrast, the Pb-6*p* orbitals cross the E_F to increase the electron density, promoting the electron transfer of the electrocatalysts. Similar to the electronic distributions, the PDOS of PdH_x are different due to the electronic modulations induced by the formation of the hydride system (Fig. 5e). Notably, Pd-4*d* orbitals become sharper when compared to that of PdPb, leading to the overall upshifting band to the E_F with enhanced electroactivity. Meanwhile, the H-1*s* orbitals are well overlapping with the Pd-4*d* orbitals, supporting the stable structures of PdH_x. For the $PdPbH_x$, the Pd-4*d* orbitals become more concentrated and closer to the E_F, which results in a slightly increased valence state induced by the electronic modulations of introduced Pb (Fig. 5f). Compared to PdPb, the Pb-6*s* orbitals remain similar while the 6*p* orbitals also become more concentrated near E_F, which benefits the *p*-*d* overlapping with Pd-4*d* orbitals to enhance electron transfer and exchange efficiency. In addition, the H-1*s* orbitals are not strongly disturbed by the Pb, which guarantees the stability of the structures. In addition, we have included two additional compositions of 4.5% and 18% for Pb and supplied H contents of 0.2 and 0.4 as comparison samples. Both electronic structures and reaction trends have also been demonstrated. Compared to $PdPbH_x$, we notice that the higher Pb and H concentrations will slightly downshift the d orbitals of Pd, which demonstrates that Pb and H compositions also influence electron transfer (Supplementary Fig. 46a–d). From the site-dependent PDOS, we notice that edge Pd atoms demonstrate higher 4 *d* orbitals than the Pd sites in PdPb (Fig. 5g). In particular, the nearby H atoms significantly improve the electroactivity of Pd sites, which benefits the direct dissociations of O_2. For the Pb sites, the Pb-6*s*,6*p* orbitals are strongly different from the bulk metal, which are attributed to the isolated states of Pb atoms in $PdPbH_x$ (Fig. 5h). Moreover, the surface and edge Pb sites display increased electron density since both 6 *s* and 6*p* orbitals shift closer to the E_F, which not only improves the overlapping with Pd-4*d* orbitals but also facilitates the electron transfer to enhance the adsorption of O_2. Then, we have summarized the d-band and p-band centers in Pd and Pb sites, respectively (Fig. 5i). From PdPb to $PdPbH_x$, the *d*-band center has gradually upshifted from E_V-2.05 eV to E_V-1.81 eV, revealing the increased electroactivity of Pd for stronger adsorption of O_2. In contrast, the downshifted *p*-band center in $PdPbH_x$ is ascribed to the contributions of Pb-6*p* orbitals becoming higher near the E_F, which promotes the electron transfer from $PdPbH_x$ to the O_2 and thus enhances the adsorption of O_2. For the introduction of Pb, we notice that further decrease or increase in the Pb compositions results in the decreases of *d*-band and *p*-band centers, indicating that a suitable Pb composition is critical to guarantee high electroactivity of Pd sites (Supplementary Fig. 46e, f). In comparison, the increasing H contents lead to the downshifted electroactivity of *d*-band and *p*-band centers towards decreasing electroactivity.

As shown in Fig. 5j and Supplementary Fig. 47, the $PdPbH_x$ displays a lower adsorption energy of O_2 than PdPb and PdH_x, indicating the stronger adsorption ability with O_2, which can promote the oxygen dissociative pathway. The increases in Pb and H contents in $PdPbH_x$ have been found to enhance the adsorption of O_2 for the ORR (Supplementary Fig. 46g). The reaction energy change of the ORR dissociative process is further investigated under both equilibrium (U = 1.23 V) and limiting potential (U_L). As shown in Fig. 5k, under the equilibrium potential of 1.23 V, both PdH_x and $PdPbH_x$ demonstrate a spontaneous tendency for the generation of 2^*O, supporting the high selectivity towards the dissociative pathways. Specifically, $PdPbH_x$ shows a smaller (RDS) energy barrier for the rate-determining step of $^*OH$ desorption, being 0.49 eV, compared to 0.56 eV of PdH_x. This demonstrates that the introduction of Pb atoms further promotes the proceeding of the oxygen dissociative pathway by reducing the dissociation barriers and desorption of *OH during the ORR. Meanwhile, the PdPb, Pd, and Pt(111) all meet large energy barriers at the initial conversion from O_2 to 2^*O, indicating the oxygen dissociative pathway was difficult to occur (Supplementary Fig. 48). For both associative and dissociative mechanisms, it is worth noting that the chemisorption of O_2 is the chemical step without any electron transfer involved, where the energy costs of O_2 dissociation cannot be alleviated by introducing the electrochemical potential[46]. Based on the computational hydrogen electrode (CHE) model, the corresponding U_L of ORR under the dissociative mechanism is evaluated to be 0.98 V and 0.95 V for $PdPbH_x$ metallenes and PdH_x metallenes, respectively. The high ORR performance of $PdPbH_x$ metallenes is ascribed to the fast dissociation step, while the high barrier of the dissociation in PdPb metallenes significantly limits the kinetics of the ORR. The bulk Pt and Pd metallene have significantly higher RDS barriers for the dissociative ORR mechanisms compared to $PdPbH_x$ (Supplementary Fig. 48). The dissociation barrier

https://doi.org/10.1038/s41467-025-60400-5

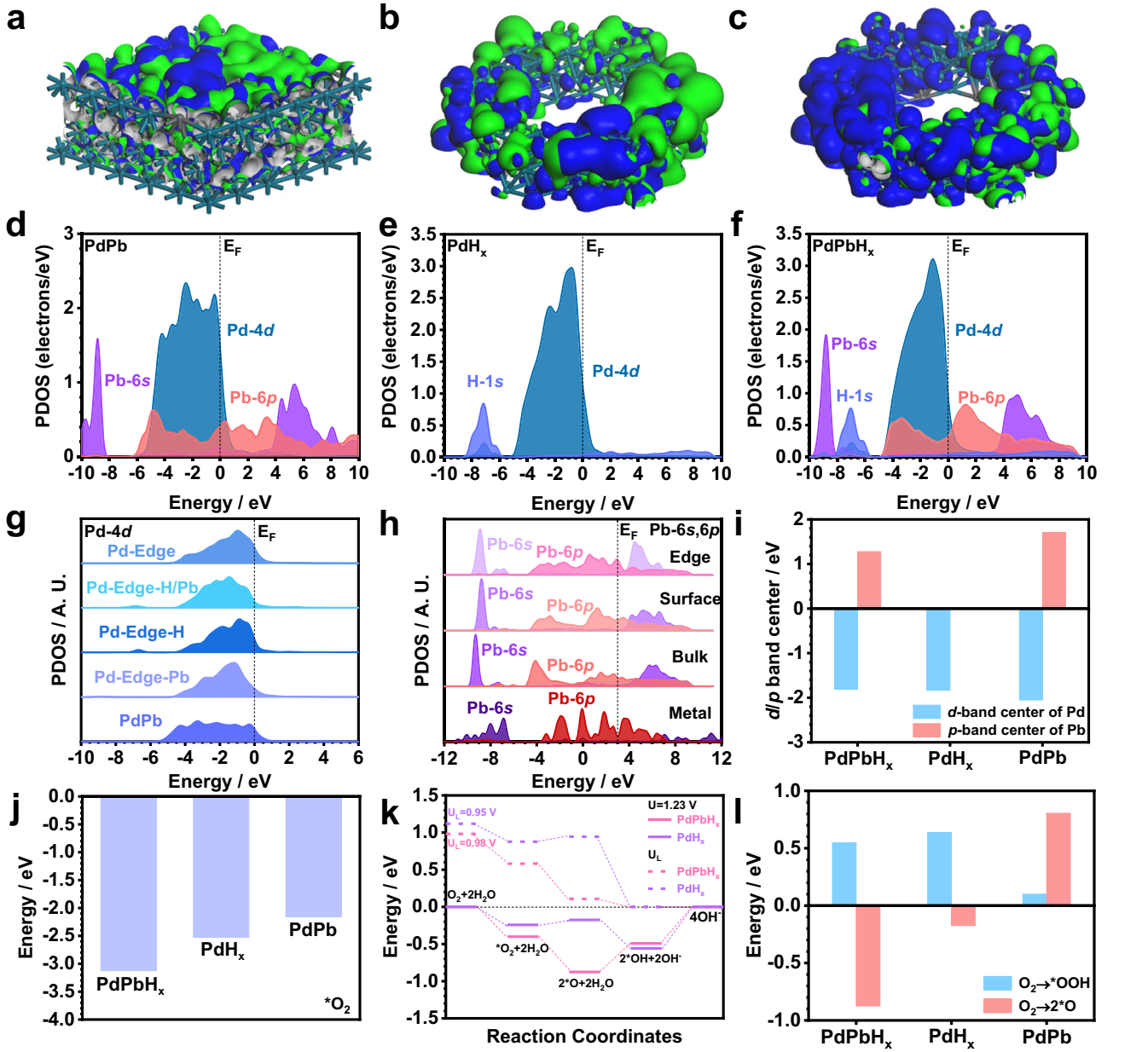

Fig. 5 | Theoretical investigations regarding the electronic structures and reaction trends for ORR. The electronic distributions of bonding and anti-bonding orbitals near the Fermi level of (**a**) PdPb, (**b**) PdH_x, and (**c**) $PdPbH_x$. Olive balls = Pd, Grey balls= Pb, and White balls = H. Blue isosurface = bonding orbitals, and green isosurface = anti-bonding orbitals. The PDOSs of (**d**) PdPb, (**e**) PdH_x, and (**f**) $PdPbH_x$. The site-dependent PDOSs of (**g**) Pd-4*d* and (**h**) Pb-6*s*, 6*p* of $PdPbH_x$. **i** The d-band and p-band center evolutions of Pd and Pb in different electrocatalysts. **j** The comparison of adsorption energies for O_2. **k** The reaction energy trends of ORR through the dissociative pathway for $PdPbH_x$ metallenes, and PdH_x metallenes. **l** The comparison of ΔG of $^*O_2 \rightarrow {}^*OOH$ and $^*O_2 \rightarrow 2^*O$ reaction steps for $PdPbH_x$ metallenes, PdH_x metallenes and PdPb metallenes. Source data are provided as a Source Data file.

of O_2 further confirms that $PdPbH_x$ exhibits the smallest kinetic barrier of 0.08 eV to guarantee the efficient dissociative ORR (Supplementary Fig. 49a). In order to more intuitively compare the difference of ORR pathways on three catalysts, the ΔG changes of the associative pathways are demonstrated (Supplementary Fig. 49b). The first protonation from chemisorbed $^*O_2$ to *OOH is the potential limiting step for $PdPbH_x$ metallenes, PdH_x metallenes, and PdPb metallenes. In contrast, the Pd and Pt(111) exhibit the last desorption step of $^*OH$ as the potential limiting step. For both $PdPbH_x$ and PdH_x, the limiting potential of the dissociative pathway is much higher than that of the associative pathway, supporting the domination of the dissociative pathway during the ORR (Supplementary Fig. 49c). In comparison, the limiting potential for PdPb, Pd, and Pt(111) display a converse trend, where the associative pathways are more feasible with higher limiting potentials.

To compare the selectivity of different ORR pathways, the energy difference of $O_2 \rightarrow 2^*O$ and $^*O_2 \rightarrow {}^*OOH$ were summarized for PdPb, PdH_x and $PdPbH_x$ (Fig. 5l). For PdPb, the ΔG of $^*O_2 \rightarrow {}^*OOH$ was 0.10 eV while the ΔG of $^*O_2 \rightarrow 2^*O$ was 0.81 eV, demonstrating that oxygen was difficult to dissociate on PdPb. Different from PdPb, the ΔG of $^*O_2 \rightarrow 2^*O$ of PdH_x and $PdPbH_x$ were −0.17 eV and −0.87 eV, which is far below their ΔG of $^*O_2 \rightarrow {}^*OOH$ (0.55 eV and 0.64 eV, respectively). The huge energy difference illustrates that PdH_x and $PdPbH_x$ prefer to occur in the oxygen dissociative pathway, proving that the oxygen was more easily dissociated on $PdPbH_x$. In addition, the RDS barrier comparisons further reveal the ORR mechanism preference. It was found that $PdPbH_x$ exhibits the smallest overall RDS barriers, supporting its superior ORR performances (Supplementary Fig. 49d). For both $PdPbH_x$ and PdH_x, the smaller difference of RDS barriers between

dissociative and associative mechanisms lead to the co-existence of both ORR mechanisms as observed by experimental characterizations in Fig. 4. On the other hand, associative mechanisms strongly prevail in PdPb, Pd metallene, and Pt (111) owing to their significantly lower RDS barriers. With the modulations of Pb and H compositions, the corresponding ΔG of $^*O_2 \rightarrow 2^*O$ and $^*O_2 \rightarrow {}^*OOH$ are also affected (Supplementary Fig. 46h–i). The Pb introduction is able to strengthen the adsorption of O_2 to accelerate the dissociative mechanism, where a suitable composition optimizes the RDS barrier to reach superior ORR. The H introduction modulates the reaction trends of dissociative mechanisms, while its impact on associative mechanisms is limited. It is essential to optimize both Pb and H contents to ensure the highest electroactivity of the surface Pd sites during electrocatalysis. Additionally, the oxygen coverage on $PdPbH_x$ also affects the ORR trends (Supplementary Fig. 50a, b). Higher oxygen coverage results in higher energy barriers for direct dissociation mechanisms and favors the associative mechanisms (Supplementary Fig. 50c, d). As the oxygen coverage gradually increases, the surface electroactivity is weakened, especially for the adsorption of O_2, which limits the direct dissociation of adsorbed O_2, leading to increasing energy barriers for the dissociative mechanisms. These are attributed to the electronic modulations on the Pd sites by the O coverage (Supplementary Fig. 50e, f)[54]. For Pd-4*d* orbitals, we notice the downshifting trend with the oxygen coverage increases, which will reduce the overall electroactivity and binding strengths. The broad O-2*p* orbitals cover from E_V-6.0 eV to E_V + 2.0 eV, which will overlap with Pb-6*p* and Pd-4*d* orbitals to further modulate the surface electroactivity towards ORR. The decreasing *d*-band centers of Pd lead to the reduced adsorption strengths of O_2 to promote the associative mechanism. These results indicate that the dissociative mechanism dominates the ORR at low oxygen coverage for $PdPbH_x$ while the associative mechanism becomes more feasible at high oxygen coverage.

Discussion

In summary, the synthesis of $PdMH_x$ (M = In, Sn, Pb) metallenes, with the inclusion of single *p*-block atoms and interstitial H atoms in the lattice of Pd metallenes, has led to the development of a highly efficient alkaline ORR catalyst. Among them, $PdPbH_x$ metallenes demonstrated a high MA of 1.36 A mg^{-1} under 0.95 V. This value is 46.9 times higher than that of commercial Pt/C and surpasses all previously Pd-based reported ORR catalysts. Additionally, the $PdPbH_x$ metallenes exhibited good durability, with no significant reduction in activity even after 50,000 potential-scanning cycles. The in situ ATR-FTIR spectra revealed that the presence of interstitial H atoms triggered the oxygen dissociative pathway, while the inclusion of Pb atoms enhanced the initial adsorption capacity of O_2 on Pd metallenes, promoting the oxygen dissociative pathway. DFT calculations further demonstrated that the incorporation of hydride systems is able to optimize the electronic structures of $PdPbH_x$, and the confined single Pb atoms facilitated electron transfer through *p-d* orbital coupling. This resulted in enhanced O_2 adsorption and subsequent dissociation to $^*O$ with lower energy barriers when compared to the conventional conversion to $^*OOH$, providing a more efficient pathway for the ORR. Our findings highlight the successful regulation of the ORR pathway through co-doping metal and non-metal atoms, offering valuable insights for the design of highly efficient electrocatalysts.

Methods

Materials

Palladium acetylacetonate ($Pd(acac)_2$, 99%) was purchased from Sigma-Aldrich (USA). Plumbum acetylacetonate ($Pb(acac)_2$, 99%), Indium acetylacetonate ($In(acac)_3$, 99%) and Tin acetylacetonate ($Sn(acac)_2$, 99%) were purchased from Aladdin (China). Commercial Pt/C catalyst (20 wt. %) was obtained from Johnson Mattkey (UK). Polyvinylpyrrolidone (PVP MW = 40000, K30) was obtained from Aladdin Co., Ltd. (China). Hexadecyl trimethyl ammonium bromide (CTAB, 99%) were obtained from Shanghai Macklin Biochemical Co., Ltd. (China). N,N-dimethylformamide (DMF, AR), potassium hydroxide (KOH, AR), isopropanol ($CH_3CH_2CH_2OH$) and ethanol (CH_3CH_2OH, AR) were all purchased from Sinopharm Chemical Reagent Co., Ltd. (China). Carbon monoxide (ultra-purity) was purchased from Xin'guang Gas Co., Ltd. (Changchun, China). Nafion-ethanol solution was obtained from Adamas-beta Chemical (Switzerland). Milli-Q deionized water (DI water, 18.2 MΩ cm^{-1}) was used in all experiments. All reagents were used as received without further purification.

Synthesis of $PdMH_x$ metallenes

The typical synthetic method of $PdPbH_x$ metallenes: Pd metallenes to be used as the seed were synthesized by using a modified protocol previously reported work[55]. First step: 50 mg $Pd(acac)_2$, 160 mg PVP, and 185 mg CTAB were added to the mixed solution with 10 mL DMF and 2 mL water with magnetic stirring. The resulting homogeneous yellow solution as transferred into a Schlenk flask, and charged with CO gas. Then the flask was immediately shifted into an oil bath that had been pre-heated to a temperature of 40 °C and held for 12 h. Second step: 20 mg $Pd(acac)_2$ and 10 mg $Pb(acac)_2$ were added to the above solution. After the solution is ultrasonically mixed, and charged with CO gas. Then the flask was immediately shifted into an oil bath that had been pre-heated to a temperature of 40 °C and held for 12 h again to obtain PdPb metallenes via epitaxial growth. The obtained PdPb metallenes were separated by centrifugation and washed three times with ethanol. Third step: PdPb metallenes were dispersed in the 15 mL DMF and transferred into a 25 mL Teflon-lined stainless steel autoclave. The autoclave was heated at 160 °C for 4 h. The final product was collected by centrifugation (4695 g, 10 min) and washed three times with ethanol. The $PdInH_x$ and $PdSnH_x$ metallenes were synthesized via a similar procedure, except that $In(acac)_3$ (10.0 mg) and $Sn(acac)_2$ (10.0 mg) were utilized instead, respectively.

Synthesis of PdH_x metallenes

The synthesis step was the same as $PdPbH_x$ metallenes except that $Pb(acac)_2$ was removed from the second step.

Synthesis of PdPb metallenes

The synthesis step was the same as $PdPbH_x$ metallenes except the third step was removed.

Material characterizations

Transmission electron microscopy (TEM) and high-resolution transmission electron microscopy (HRTEM) were performed on a JEOL JEM-2100F transmission electron microscope (Japan). Scanning transmission electron microscopy (STEM) images and corresponding energy-disperse X-ray spectroscopy (EDS) mapping, and electron-energy loss spectroscopy (EELS) were obtained by a JEOL ARM200CF (Japan). For atomic force microscopy (AFM) characterization, samples were deposited onto mica wafers and analyzed in tapping mode under ambient air conditions via the ScanAsyst (Dimension Icon, Veeco Instruments/Bruker, Germany). X-ray photoelectron spectroscopy (XPS) data were collected using a Thermo Fisher Scientific ESCALAB-250 instrument (USA) with a monochromatic Al-Kα radiation source (1486.6 eV) and a hemispherical detector (0.1 eV energy resolution). Inductively coupled plasma atomic emission spectroscopy (ICP-AES) measurements and X-ray diffraction (XRD) patterns were conducted using an ELAN 9000/DRC system and a Bragg-Brentano diffractometer (D8-tools, Germany), respectively. X-ray absorption spectra of the Pd K-edge and Pb L3-edge were collected in both transmission (for Pd foil, Pb foil, PdO, and PbO) and fluorescence (for the sample) mode at Shanghai Synchrotron Radiation Facility (SSRF) on beamline BL14W1.

Electrochemical measurements

The as-prepared Pd-based metallenes are stored in an ethanol solution, with the concentration of Pd determined by ICP-AES to be approximately 1.0 mg_{Pd}/mL. For catalytic evaluation, 5 mL of metallene solution (containing 5 mg of Pd) and 45 mg Ketjen carbon were added in 45 mL ethanol and then sonicated for 20 min to achieve a homogeneous dispersion. Subsequently, the sonicated mixture is subjected to an additional minute of oscillation. The ultrasonic and oscillating processes were repeated three times to ensure the catalyst was fully loaded on the Ketjen carbon. Then the solution was centrifuged and poured off the supernatant, dried in a 60 °C vacuum drying oven for 12 h. For the preparation of the electrochemical test catalyst ink, 1 mg of the as-synthesized $PdPbH_x$ metallenes/C powder was dispersed into a 1 mL mixture consisting of 750 µL deionized water, 245 µL isopropanol, and 5 µL of 5 wt% Nafion solution. This mixture underwent 30 min of sonication in an ice-water bath to form a homogeneous dispersion. The resulting uniform catalyst ink was then utilized for fabricating the working electrode. As a comparative benchmark, the commercial 20 wt% Pt/C catalyst from Johnson-Matthey was employed.

Electrochemical measurements were conducted using a three-electrode configuration on an Autolab electrochemical workstation. The working electrode consisted of a catalyst-coated glassy carbon electrode (GCE, 5 mm diameter) mounted on a rotator, while a platinum sheet (1.0 cm^2) served as the counter electrode and a Hg/HgO electrode acted as the reference electrode. The preparation method of 0.1 M KOH electrolyte is as follows: dissolving 2.8 g of KOH in 500 mL of deionized water, followed by ultrasonication to ensure a uniform solution. The 0.1 M KOH electrolyte was freshly prepared before electrochemical measurements and stored in a sealed container at 25 °C. The calibration potential was approximately equal to the calculated value based on the Nernst equation (the measured pH value of 0.1 M KOH solution was 13.3 ± 0.3 under the actual ORR testing process). All the potentials were converted to the potentials referring to the RHE. Prior to catalyst deposition, the glassy carbon electrode was sequentially polished with alumina polishing slurries, rinsed thoroughly with deionized water, and left to air-dry naturally. Subsequently, 10 µL of the ink was dropped on a GCE to form a smooth thin film, yielding a Pd loading of 1.0 µg (5.1 µg cm^{-2}). For Commercial Pt/C, the Pt loading of 2.0 µg (10.2 µg cm^{-2}) were added to the GCE to obtain a similar limited diffusion current with other catalysts. The ECSA ($m^2 \cdot g^{-1}_{PGMs}$) of the catalysts was calculated according to the equation:

$$ECSA = \frac{Q}{mq} \quad (1)$$

where Q represents the surface charge for oxygen desorption, q is the charge required for the reduction of a PdO monolayer (424 µC cm^{-2}) and m is the Pd loading amount. For ECSA, the cyclic voltammogram (CV) was obtained in N_2-saturated 0.1 M KOH with a scan rate of 50 mV s^{-1}. ORR polarization curves were measured in an O_2-saturated 0.1 M KOH electrolyte, employing a scan rate of 10 mV s^{-1} and a rotation speed of 1,600 rpm. iR-correction has been applied to the recorded ORR curves before determining the kinetic current (I_k) based on the Koutecký-Levich equation:

$$I_k = \frac{I_d * I}{I_d - I} \quad (2)$$

where I_d is the limiting current density, and I is the measured current density at 0.9/0.95 V versus RHE. For each catalyst, the specific activity and mass activity were derived by normalizing the kinetic current against the corresponding electrochemical active surface area (ECSA) and the metal (platinum group metals, PGMs) mass, respectively. All activities were obtained by averaging at least three patches of materials and corresponding performances.

In the accelerated durability tests, a graphite rod was indeed used as the counter electrode, which could prevent Pt from the counter electrode dissolving and redeposition on the working electrode during the long hours of the test. The accelerated durability tests were conducted by cycling between 0.6 V and 1.0 V versus RHE at 200 mV s^{-1} for 50,000 cycles. For comparison, the ORR performance of the commercial Pt/C was also measured through similar procedures.

EIS measurements were conducted at the open-circuit potential (OCP) by applying a sinusoidal AC perturbation with a frequency range from 100 kHz to 10 mHz and an amplitude of 10 mV. Prior to the measurement, the OCP was stabilized with a fluctuation of less than 1 mV/min. All recorded potentials were corrected for ohmic drop using iR compensation (R_s = 40 ± 5 Ω in 0.1 M KOH).

Zn-air battery test

The anode and cathode have used a polished zinc foil (0.5 mm thickness) and a catalyst-coated hydrophobic carbon paper (Spring-P2), respectively. The electrolyte uses a solution composed of 0.2 M $Zn(AC)_2$ and 6 M KOH. The catalyst ink was prepared by ultrasonically mixing 3 mg catalysts and 1 mg Vulcan XC 72 carbon in 600 µL dispersion solution (volume ratio of water/isopropanol/Nafion =44.2/55.2/0.6). To fabricate the cathode, the catalyst ink was then deposited onto the carbon paper via drop-casting, with a catalyst loading of 1.0 mg cm^{-2} (0.1 $mg_{Pd\ or\ Pt}$ per cm^2). By using the LAND CT3002A instrument, the discharge polarization curve was recorded.

Membrane electrode assembly (MEA) fabrication and fuel cell tests

The catalyst at the cathode and anode is 20 wt% $PdPbH_x$/C or commercial 20 wt% Pt/C with a metal loading of 0.3 $mg_{Pd/Pt}$ cm^{-2} and commercial 60 wt% PtRu/C (Shanghai Hesen Electric Co., Ltd) with a metal loading of 0.6 mg PtRu mg_{PtRu} cm^{-2}, respectively. The cathode ink was obtained by mixing the catalyst powder with water, isopropanol (volume ratio of 1:10), and 30 wt% home-made ionomer[56] ($m_{ionomer}/(m_{ionomer}+ m_{catalyst})$ = 30 wt%). The anode slurry was also prepared using the same method mentioned above, except that the amount of ionomer is 23 wt% ($m_{ionomer}/(m_{ionomer}+ m_{catalyst})$ = 23 wt%).

A catalyst-coated membrane (CCM, ~4 cm^2) was prepared by sequentially spraying cathodic and anodic slurry onto each side of the commercial membrane (Alkymer® W-25 alkaline membrane. Thickness: 25 µm). Afterwards, the CCM was immersed in 1 M NaOH aq. at 60 °C for 24 h (to promote the ion exchanging Cl^- with OH^- in alkaline conditions, ensuring the membrane's suitability for alkaline environments), followed by washing 3 times with deionized water, and then MEA was fabricated by sandwiching the CCM between two carbon papers (Sunrise Power Co., Ltd.) at 25 °C and a gauge pressure of 0.2 MPa for 2 min.

The single cell performance was conducted on a home-made test system at 80 °C by feeding O_2/H_2 (100% relative humidity, RH) with a 400/400 mL min^{-1} flow rate at the cathode and anode. A durability test was performed at 80 °C and 100 mA cm^{-2}.

XAFS data analysis

The collected XAFS data underwent systematic processing in Athena software (version 0.9.26), involving background subtraction, pre-edge linear correction, and post-edge linear calibration. Subsequent Fourier transform fitting analysis was conducted using Artemis (version 0.9.26). For Pd fitting, the parameters were configured as: k^3-weighting, k-range from 3 to ~12 $Å^{-1}$, and R-range from 1 to ~3 Å; while for Pb fitting, the k-range was adjusted to 2 to ~10 $Å^{-1}$ (with the R-range maintained at 1 to ~3 Å). Four critical parameters- coordination number (CN), bond length (R), Debye-Waller factor (σ^2), and E_0 shift (ΔE_0)- were optimized without imposing fixed constraints or correlation limitations. For Wavelet Transform (WT) analysis, the χ(k) data extracted from Athena was imported into the Hama Fortran code. The specific

parameters for this analysis were defined as: R-range of 1–4 Å; k-range of 0– ~ 13 $Å^{-1}$ (for Pd) and 0– ~ 10 $Å^{-1}$ (for Pb); k-weight value of 2; and a Morlet mother wavelet with κ = 10 and σ = 1, which facilitated comprehensive distribution characterization.

XRD data refinement

The XRD data were refined using the Rietveld method with the HighScore software to optimize the reliability and structural parameters.

Quasi in situ XPS measurement

The $PdPbH_x$ sample was dropped onto three carbon papers, each with a Pd loading of 1 mg. These carbon papers were then subjected to chronoamperometry (i-t) tests at constant potentials of 0.7 V, 0.9 V, and 1.1 V for 200 s, respectively. Upon completion of the tests, the carbon papers were promptly transferred into centrifuge tubes and sealed under an argon atmosphere to prevent oxidation. Subsequently, XPS characterization was conducted to analyze the chemical states of the samples.

In situ ATR-FTIR measurement

Surface-enhanced infrared absorption spectroscopy (SEIRAS) in attenuated total reflection (ATR) configuration was adopted for the measurements. Electrochemical ATR-SEIRAS characterization was performed using a Thermo Nicolet 8700 spectrometer, which was outfitted with a liquid nitrogen-cooled MCT detector. During the testing process, 0.1 M KOH was used as the electrolyte, which, due to the low alkalinity, will not cause the gold film to detach from the prism. Additionally, to avoid any impact from multiple tests on the gold film, we only performed one oxygen reduction test at full voltage on each gold film. 30 μL of the catalyst ink was applied onto the gold-film working electrode and left to air-dry. Subsequently, the ink-coated silicon column- functioning as the prism with dimensions of 10 mm radius and 25 mm height- was integrated into a custom-built spectro-electrochemical cell to serve as the working electrode. The Hg/HgO was used as the reference electrode, which was introduced near the working electrode via a Luggin capillary while the Pt mesh (1 cm × 1 cm) served as the counter electrode. All spectra were normalized using the differential reflectance formula:

$$\frac{\Delta R}{R} = \frac{E_s - E_R}{E_R} \tag{3}$$

where Es and E_R represent the sample and reference spectra, respectively. For the spectra results, all the spectral resolutions were 4 cm^{-1}. The reference spectrum was recorded at 0 mV and the sample spectra were collected at the potentials from 1000 mV to 1600 mV (vs RHE) with the successive potential step of 100 mV.

Calculation setup

In this work, all the density functional theory (DFT) calculations are carried out by the CASTEP package to investigate the electronic structures and reaction trends of PdPb, PdH_x, and $PdPbH_x$ for ORR[57]. In particular, we have selected the generalized gradient approximation (GGA) and Perdew-Burke-Ernzerhof (PBE) functionals to supply accurate descriptions of the exchange-correlation interactions[58–60]. We have selected the ultrasoft pseudopotentials with ultrafine quality for the plane-wave cutoff energy, which has been set to 380 eV by default. For further increases of the cutoff energy to 400 eV, the total energy of $PdPbH_x$ test model only shifts a very minor scale of around 11 meV, which justifies the use of this cutoff energy setting. The Broyden-Fletcher-Goldfarb-Shannon algorithm with the selection of coarse k-point has been applied for the energy minimization processes in this work[61]. The PdPb surface has been cleaved from the (111) surface of Pd with a four-layer thickness in a 5 × 5 × 1 supercell, where 9% Pd atoms are replaced by the Pb atoms. For PdH_x, the metallene structure has been cleaved from the (111) surface of PdH with a three-layer thickness, where x is close to 0.3. The $PdPbH_x$ is further constructed by replacing 9% Pd atoms with Pb atoms, which matches the experimental characterizations. The Pd metallene has been cleaved from the Pd(111) surface with four-layer thicknesses in a 5 × 5 × 1 supercell, where the PdPb metallene is constructed by replacing 9% Pd atoms with the Pb atoms. The bulk Pt surface is cleaved from the Pt(111) surface with an eight-layer thickness in a 5 × 5 × 1 supercell. The structures are supplied in Supplementary Data 1. For all the surfaces, 20 Å vacuum space has been introduced in the z-axis to guarantee complete relaxation.

To achieve sufficient geometry optimizations, a series of strict convergence criteria are applied, which include that the Hellmann-Feynman forces should be converged to less than 0.001 eV/Å, the total energy difference should be converged to smaller than 5×10^{-5} eV/atom, and the maximum displacement for each atom should be smaller than 0.005 Å. In this work, we have performed DFT calculations based on the computational hydrogen electrode (CHE) model proposed by Nørskov et al. [18] The equilibrium potential on a reversible hydrogen electrode (RHE) is set to be the reference of applied potential. When an electrode potential U is applied, the chemical potential of the electron will be reduced by *eU*, which has been considered in all states involving an electron in the electrode. The limiting potential U_L is then determined when all the reaction steps become spontaneous. The free energy (ΔG) is calculated based on

$$\Delta G = \Delta E + \Delta ZPE - T\Delta S \tag{4}$$

where the ΔZPE and ΔS are the changes of the zero-point energy and entropy, respectively at T = 298.15 K and 1 atm. The MD simulations have been carried out under 298 K and NVT mode in $PdPbH_x$, PdH_x, and PdPb metallene for 5 ps, where each step is 1 fs with a total of 5000 simulation steps (Supplementary Data 1).

Data availability

The data generated in this study are provided in the Supplementary Information and Source Data file. Source data are provided in this paper. Source data are provided with this paper.

References

1. Debe, M. Electrocatalyst approaches and challenges for automotive fuel cells. *Nature* **486**, 43–51 (2012).
2. Lin, F., Li, M., Zeng, L., Luo, M. & Guo, S. Intermetallic nanocrystals for fuel-cells-based electrocatalysis. *Chem. Rev.* **123**, 12507–12593 (2023).
3. Gasteiger, H. et al. Activity benchmarks and requirements for Pt, Pt-alloy, and non-Pt oxygen reduction catalysts for PEMFCs. *Appl. Catal. B-Environ.* **56**, 9–35 (2005).
4. Tian, X., Lu, X., Xia, B. & Lou, X. Advanced electrocatalysts for the oxygen reduction reaction in energy conversion technologies. *Joule* **4**, 45–68 (2020).
5. Wang, Q., Kaushik, S., Xiao, X. & Xu, Q. Sustainable zinc-air battery chemistry: advances, challenges and prospects. *Chem. Soc. Rev.* **52**, 6139–6190 (2023).
6. Seh, Z. et al. Combining theory and experiment in electrocatalysis: insights into materials design. *Science* **355**, eaad4998 (2017).
7. Kattel, S. & Wang, G. Reaction pathway for oxygen reduction on FeN_4 embedded graphene. *J. Phys. Chem. C.* **5**, 452–456 (2014).
8. Kulkarni, A., Siahrostami, S., Patel, A. & Nørskov, J. Understanding catalytic activity trends in the oxygen reduction reaction. *Chem. Rev.* **118**, 2302–2312 (2018).
9. Liang, J. et al. Gas-balancing adsorption strategy towards noble-metal-based nanowire electrocatalysts. *Nat. Catal.* **7**, 719–732 (2024).

10. Sun, K. et al. Co $(CN)_3$ catalysts with well-defined coordination structure for the oxygen reduction reaction. *Nat. Catal.* **6**, 1164–1173 (2023).
11. Shao, R. et al. Promoting ordering degree of intermetallic fuel cell catalysts by low-melting-point metal doping. *Nat. Commun.* **14**, 5896 (2023).
12. Huang, L. et al. An integrated platinum-nanocarbon electrocatalyst for efficient oxygen reduction. *Nat. Commun.* **13**, 7270 (2022).
13. Bu, L. et al. Three-dimensional porous platinum-tellurium-rhodium surface/interface achieve remarkable practical fuel cell catalysis. *Energy Environ. Sci.* **15**, 3877–3890 (2022).
14. Wu, Q. et al. Ultra-dense carbon defects as highly active sites for oxygen reduction catalysis. *Chem* **8**, 2715–2733 (2022).
15. Xiao, F. et al. Atomically dispersed Pt and Fe sites and Pt-Fe nanoparticles for durable proton exchange membrane fuel cells. *Nat. Catal.* **5**, 503–512 (2022).
16. Koper, M. Theory of multiple proton-electron transfer reactions and its implications for electrocatalysis. *Chem. Sci.* **4**, 2710–2723 (2013).
17. Li, H. et al. Analysis of the limitations in the oxygen reduction activity of transition metal oxide surfaces. *Nat. Catal.* **4**, 463–468 (2021).
18. Nørskov, J. et al. Origin of the overpotential for oxygen reduction at a fuel-cell cathode. *J. Phys. Chem. B* **108**, 17886–17892 (2004).
19. Zhang, N. et al. High-density planar-like Fe_2N_6 structure catalyzes efficient oxygen reduction. *Matter* **3**, 509–521 (2020).
20. Su, H. et al. Dynamic evolution of solid-liquid electrochemical interfaces over single-atom active sites. *J. Am. Chem. Soc.* **142**, 12306–12313 (2020).
21. Liu, M. et al. Avoiding sabatier's limitation on spatially correlated Pt-Mn atomic pair sites for oxygen electroreduction. *J. Am. Chem. Soc.* **145**, 25252–25263 (2023).
22. Zhou, W. et al. Regulating the scaling relationship for high catalytic kinetics and selectivity of the oxygen reduction reaction. *Nat. Commun.* **13**, 6414 (2022).
23. Luo, M. et al. PdMo bimetallene for oxygen reduction catalysis. *Nature* **574**, 81–85 (2019).
24. Li, H. et al. Oxidative stability matters: A case study of palladium hydride nanosheets for alkaline fuel cells. *J. Am. Chem. Soc.* **144**, 8106–8114 (2022).
25. Tao, L. et al. Precise synthetic control of exclusive ligand effect boosts oxygen reduction catalysis. *Nat. Commun.* **14**, 6893 (2023).
26. Xie, L. et al. Modulating the bader charge transfer in single *p*-block atoms doped Pd metallene for enhanced oxygen reduction electrocatalysis. *Angew. Chem. Int. Ed.* **63**, e202407658 (2024).
27. Lin, F. et al. Local coordination regulation through tuning atomic-scale cavities of Pd metallene toward efficient oxygen reduction electrocatalysis. *Adv. Mater.* **34**, 2202084 (2022).
28. Qiu, Y. et al. Atomically dispersed CrO_x on Pd metallene for CO-resistant methanol oxidation. *Nano lett.* **23**, 9555–9562 (2023).
29. Wu, G. et al. In-plane strain engineering in ultrathin noble metal nanosheets boosts the intrinsic electrocatalytic hydrogen evolution activity. *Nat. Commun.* **13**, 4200 (2022).
30. Xie, M. et al. Intermetallic single-atom alloy In-Pd bimetallene for neutral electrosynthesis of ammonia from nitrate. *J. Am. Chem. Soc.* **145**, 13957–13967 (2023).
31. Lv, F. et al. A highly efficient atomically thin curved PdIr bimetallene electrocatalyst. *Natl Sci. Rev.* **8**, nwab019 (2021).
32. Yu, H. et al. Defect-rich porous palladium metallene for enhanced alkaline oxygen reduction electrocatalysis. *Angew. Chem. Int. Ed.* **60**, 12027–12031 (2021).
33. Huang, S. et al. Sublayer stable Fe dopant in porous Pd metallene boosts oxygen reduction reaction. *ACS Nano* **16**, 522–532 (2022).
34. Wang, L. et al. Tunable intrinsic strain in two-dimensional transition metal electrocatalysts. *Science* **363**, 870–874 (2019).
35. Wang, Y. et al. A universal synthesis of ultrathin Pd-based nanorings for efficient ethanol electrooxidation. *Mater. Horiz.* **10**, 1416–1424 (2023).
36. Bukharaev, A., Berdunov, N., Ovchinnikov, D. & Salikhov, K. Three-dimensional probe and surface reconstruction for atomic force microscopy using a deconvolution algorithm. *Scanning Microsc. Int* **12**, 225–234 (1998).
37. Markiewicz, P. & Cynthia, M. Atomic force microscopy probe tip visualization and improvement of images using a simple deconvolution procedure. *Langmuir* **10**, 5–7 (1994).
38. Fan, J. et al. Ligand-confined two-dimensional rhodium hydride boosts hydrogen evolution. *Matter* **6**, 1–12 (2023).
39. Hanneken, J., Baker, D., Conradi, M. & Eastman, J. NMR study of the nanocrystalline palladium-hydrogen system. *J. Alloy Compd.* **330**, 714–717 (2022).
40. Baldi, A., Narayan, T., Koh, A. & Dionne, J. In situ detection of hydrogen-induced phase transitions in individual palladium nanocrystals. *Nat. Mater.* **13**, 1143–1148 (2014).
41. Zhao, Z. et al. Synthesis of stable shape-controlled catalytically active β-palladium hydride. *J. Am. Chem. Soc.* **137**, 15672–15675 (2015).
42. Fan, X. et al. Surface-enriched single-Bi-atoms tailoring of Pt nanorings for direct methanol fuel cells with ultralow-Pt-loading. *Adv. Mater.* **36**, 2313179 (2024).
43. Li, M. et al. Programmable synthesis of high-entropy nanoalloys for efficient ethanol oxidation reaction. *ACS Nano* **17**, 13659–13671 (2023).
44. Sun, Y. et al. Ultrathin PtPd-Based nanorings with abundant step atoms enhance oxygen catalysis. *Adv. Mater.* **30**, 1802136 (2018).
45. Xu, R. et al. Improving the ORR performance by enhancing the Pt oxidation resistance. *J. Catal.* **416**, 311–321 (2022).
46. Rahul, R. et al. The role of surface oxygenated-species and adsorbed hydrogen in the oxygen reduction reaction (ORR) mechanism and product selectivity on Pd-based catalysts in acid media. *Phys. Chem. Chem. Phys.* **17**, 15146–15155 (2015).
47. Chen, C. et al. Highly crystalline multimetallic nanoframes with three-dimensional electrocatalytic surfaces. *Science* **343**, 1339–1343 (2014).
48. Zhang, T. & Anderson, A. Oxygen reduction on platinum electrodes in base: Theoretical study. *Electrochim. Acta* **53**, 982–989 (2007).
49. Anderson, A., Roques, J. & Mukerjee, S. Activation energies for oxygen reduction on platinum alloys: theory and experiment. *J. Phys. Chem. B.* **109**, 1198–1203 (2005).
50. Lin, C. et al. In-situ reconstructed Ru atom array on α-MnO_2 with enhanced performance for acidic water oxidation. *Nat. Catal.* **4**, 1012–1023 (2021).
51. Wang, T. et al. Enhancing oxygen reduction electrocatalysis by tuning interfacial hydrogen bonds. *Nat. Catal.* **4**, 753–762 (2021).
52. Nayak, S., McPherson, I. & Vincent, K. Adsorbed intermediates in oxygen reduction on platinum nanoparticles observed by in situ IR spectroscopy. *Angew. Chem. Int. Ed.* **57**, 12855–12858 (2018).
53. Li, H. Scalable neutral H_2O_2 electrosynthesis by platinum diphosphide nanocrystals by regulating oxygen reduction reaction pathways. *Nat. Commun.* **11**, 3928 (2020).
54. Gomez-Marin, A., Rizo, R. & Feliu, J. Oxygen reduction reaction at Pt single crystals: a critical overview. *Catal. Sci. Technol.* **4**, 1685–1698 (2014).
55. Huang, X. et al. Freestanding palladium nanosheets with plasmonic and catalytic properties. *Nat. Nanotechnol.* **6**, 28–32 (2011).
56. Gong, S. et al. Completely methylene-free side chain enables significant microphase separation at medium IECs for fuel-cell anion exchange membranes. *ACS Appl. Mater. Interfaces* **16**, 27741–27749 (2024).

57. Clark, S. et al. First principles methods using CASTEP. *Z. Fur Kristallographie* **220**, 567–570 (2005).
58. Perdew, J. et al. Atoms, molecules, solids, and surfaces: Applications of the generalized gradient approximation for exchange and correlation. *Phys. Rev. B* **46**, 6671–6687 (1992).
59. Perdew, J., Burke, K. & Ernzerhof, M. Generalized gradient approximation made simple. *Phys. Rev. Lett.* **77**, 3865–3868 (1996).
60. Hasnip, P. & Pickard, C. Electronic energy minimisation with ultrasoft pseudopotentials. *Comput. Phys. Commun.* **174**, 24–29 (2006).
61. Head, J. & Zerner, M. A broyden-fletcher-goldfarb-shanno optimization procedure for molecular geometries. *Chem. Phys. Lett.* **122**, 264–270 (1985).

Acknowledgements

J. Fan and X. Cui acknowledged the support of the National Natural Science Foundation of China (12034002 (X.C.), 22279044 (X.C.), and 22402064 (J.F.)). B.H. acknowledged the support of the National Key R&D Program of China (2021YFA1501101), Research Grant Council of Hong Kong (15304023, 15304724, C1003-23Y), National Natural Science Foundation of China/Research Grant Council of Hong Kong Joint Research Scheme (N_PolyU502/21), the National Natural Science Foundation of China/Research Grants Council of Hong Kong Collaborative Research Scheme (CRS_PolyU504/22), the Shenzhen Fundamental Research Scheme-General Program (JCYJ20220531090807017), and the Natural Science Foundation of Guangdong Province (2023A1515012219).

Author contributions

J.F., B.H. and X.C. supervised the execution of the overall project. Y.Q. designed and performed the synthetic and electrochemical experiments, characterized the catalyst, and analyzed the data. M.S. and B.H. conducted the DFT calculations. J.W. assisted with the idea design of catalysts. S.W. assisted with the data analysis. H.H. and X.Z. assisted with the electrochemical ORR tests. D.J. assisted with the calculations of the ORR mechanism. S.X. assisted with the drawing of the schematic diagram. D.W. assisted with the ssNMR tests. X.G. and Wei Z. performed the atomic-resolution HAADF-STEM tests. C.C. and Y. S. performed the alkaline H_2-O_2 fuel cell test. Weitao Z. assisted with the paper writing. The results of the manuscript were discussed by all authors.

Competing interests

The authors declare no competing interests.

Additional information

Supplementary information The online version contains supplementary material available at https://doi.org/10.1038/s41467-025-60400-5.

Correspondence and requests for materials should be addressed to Jinchang Fan, Bolong Huang or Xiaoqiang Cui.

Peer review information *Nature Communications* thanks Zhao Cai and the other, anonymous, reviewer(s) for their contribution to the peer review of this work. A peer review file is available.